Catalysis Science & Technology

ROYAL SOCIETY OF CHEMISTRY

PAPER

View Article Online
View Journal | View Issue

Cite this: *Catal. Sci. Technol.*, 2026, **16**, 2716

Facet-dependent metal–support interactions in cobalt–ceria binary oxides: linking ceria morphology (rods *vs.* cubes) to redox behaviour and CO oxidation

Agapi Orfanoudaki, [a] Maria Lykaki, [a] Angelos K. Bonis,[b] Shailza Saini,[b] George Dury,[c] Greg A. Mutch, [c] Evangelos I. Papaioannou, [c] Kalliopi Kousi [b] and Michalis Konsolakis *[a]

Ceria-based binary oxides are widely employed in heterogeneous catalysis owing to their versatile applications and the fundamental interest stemming from their distinctive metal–support interactions. However, structural and surface parameters of ceria can significantly influence the redox and structural properties of mixed oxides, thereby affecting their catalytic performance. In this study, we investigate the effect of ceria morphology, *i.e.* nanorods (NR) and nanocubes (NC), on the intrinsic properties and interfacial interactions of cobalt–ceria catalysts, using CO oxidation as a probe reaction. Both bare ceria and cobalt/ceria samplers were comparatively characterized by various techniques such as N_2 physisorption, X-ray diffraction (XRD), scanning and transmission electron microscopy (SEM/TEM), temperature-programmed reduction (TPR), X-ray photoelectron spectroscopy (XPS), Raman analysis and dynamic thermogravimetric analysis (TGA) under reaction conditions, revealing the interrelationship among ceria morphology, metal dispersion, reducibility, and catalytic activity. Specifically, ceria nanorods—predominantly exposing the {100} and {110} facets—exhibit enhanced textural and redox properties, which in turn lead to superior oxidation performance. The incorporation of cobalt further improves the catalytic activity, while still reflecting the performance trend of the bare supports, thereby underscoring the primary role of ceria morphology. Notably, cobalt is highly dispersed as nanoclusters across the surface of ceria nanorods, whereas it preferentially accumulates along the edges and corners of ceria nanocubes. This distinct dispersion behaviour strongly influences metal–support interactions and facilitates the stabilisation of Co^{2+} active sites over Co/CeO_2-NR, enabling complete CO conversion at *ca.* 160 °C.

Received 31st December 2025,
Accepted 3rd March 2026

DOI: 10.1039/d5cy01612f

rsc.li/catalysis

Introduction

The swift expansion of industrialization and urban development worldwide has significantly increased energy consumption, with fossil fuels still supplying more than 80% of global energy needs.[1] This reliance exacerbates environmental challenges, particularly air pollution. Among the pollutants generated, carbon monoxide (CO), results from incomplete combustion of hydrocarbon fuels and constitutes almost half of urban air contaminants in rapidly growing megacities.[2] CO not only poses serious health hazards but also contributes to atmospheric degradation, emphasizing the urgent necessity for advanced catalytic materials to control its emissions.[3] To this end, CO oxidation can be employed as a mitigation strategy while constituting a benchmark reaction to gain insight into structure–property relationships due to the well-established reaction mechanism and easiness of methodological execution.[4–6]

Among various catalytic materials, cerium oxide (CeO_2) stands out as a highly effective catalyst either as itself or as supporting carrier, due to its unique redox properties. More specifically, its remarkable oxygen storage capacity (OSC) and the facile transition between its two oxidation states (Ce^{3+} and Ce^{4+}), enable the formation and replenishment of oxygen vacancies during various reactions.[7–9] These features can be optimized through key adjustable parameters such as shape, size, electron state, chemical modifiers and metal doping, which strongly influence surface energy, defect formation, and oxygen mobility.[7]

[a] *School of Production Engineering and Management, Technical University of Crete, Chania, Greece. E-mail: mkonsolakis@tuc.gr*
[b] *School of Chemistry and Chemical Engineering, University of Surrey, Guildford, UK*
[c] *Materials, Concepts & Reaction Engineering (MatCoRE) Group, School of Engineering, Newcastle University, Newcastle upon Tyne, UK*

In view of the above, morphology control of CeO_2 nanostructures has recently attracted significant attention as a strategy to tailor catalytic performance. In particular, the nanostructured morphology of CeO_2-based catalysts affects their efficacy by controlling the three-dimensional atomic arrangement and determining the crystallographic facets exposed to reactant molecules.[10] According to literature,[9,11,12] distinct facet preferences for different CeO_2 morphologies are revealed, in which polyhedral nanoparticles predominantly expose stable {111} facets, nanocubes favour {100} facets, while nanorods present a combination of highly reactive {110} and {100} facets. This faceted orientation directly correlates with catalytic activity, as demonstrated by the study of Chen *et al.*,[13] in which ceria nanorods exhibited abundance in surface defects, oxygen vacancies and lattice oxygen, facilitating the stabilisation of Au^+ species and resulting in the optimum activity and stability towards the removal of CO and HCHO, as compared to ceria nanopolyhedra and nanocubes. In a similar manner, ceria nanorods with coexisting {100} and {110} facets provide higher CO oxidation rates than other morphological variants (*e.g.*, nanocubes, nanopolyhedra),[14] suggesting that the morphological control of surface termination has important catalytic performance implications. However, it should be noted that the exact role of exposed facets remains a subject of ongoing investigation, with some inconsistencies across studies highlighting the complexity and current relevance of this topic.[12,15,16]

Besides the key role of ceria morphology, the catalytic performance can be notably altered by the addition of a second metal, due to the peculiar metal–support interactions.[4,8,17–21] Among the numerous catalytic systems, ceria-based transition metal oxides have gained considerable attention, as alternatives to rare and expensive noble metals.[22,23] As revealed by various studies,[24–28] cobalt catalysts are considered quite promising for oxidation reactions. Especially, the combination of cobalt with ceria has shown great potential in various applications in heterogeneous catalysis, involving, among others, the oxidation of air pollutants,[29] the preferential oxidation of CO,[30,31] reforming processes,[32,33] *etc.* It has been clearly revealed that the catalytic performance of the cobalt–ceria binary system can be profoundly modified by several fine-tuning strategies, such as the use of advanced synthesis routes,[34] promotion with metal oxides,[35] special pretreatment protocols,[36,37] *etc.* In this regard, Xu *et al.*[38] showed that CeO_2–Co_3O_4 composites with a Ce/Co atomic ratio of 1 : 16 demonstrated much higher CO oxidation activity than pure CeO_2 or Co_3O_4 due to the strong interaction between the two phases. Similarly, Konsolakis *et al.*[37] showed that the reduction instead of the oxidation pretreatment of Co_3O_4/CeO_2 catalysts promotes a uniform Co–Ce distribution, creating abundant oxygen vacancies through the Ce^{3+}/Ce^{4+} and Co^{3+}/Co^{2+} redox cycles.

Furthermore, recent studies[39,40] have shown that the ceria support morphology critically affects the catalytic performance of Co_3O_4/CeO_2 in various processes. For instance, Huang *et al.*[39] revealed that Co supported on three-dimensionally ordered mesoporous CeO_2 enhances ammonia decomposition for hydrogen generation due to the high surface area and abundance in surface oxygen vacancies, as compared to nanocubes and nanotubes. Similarly, Xie *et al.*[40] showed that CeO_2 nanorods, exposing the {110}/{100} facets, facilitate the formation of Co^0 species and oxygen vacancies, thus enhancing the metal–support interactions and the CO_2 methanation performance. Also, CoO_x/CeO_2 nanorods exhibited enhanced activity in the NO reduction by CO, as compared to nanocubes and commercial nanopowders, due to their high amount of oxygen vacancy defects which facilitated oxygen migration and charge transfer.[41]

Taking into account the oxidation of CO over cobalt–ceria catalysts, Yang *et al.*[42] synthesised Co_3O_4–CeO_2 nanocomposites through various sol–gel routes, leading to the formation of ceria-supported Co_3O_4 layers, intermixed oxides, and homogeneously dispersed Co, with the CeO_2-supported Co_3O_4 layers exhibiting the optimum activity and stability. Hollow multishelled Co_3O_4–CeO_{2-x} structures showed good CO oxidation activity with complete CO conversion at 166.9 °C and stability in a period of 100 h due to their abundance in active sites and the synergism among the shells.[43] Moreover, rod-shaped ceria catalysts doped with different transition metals (Mn, Co, Ni) were synthesised through the hydrothermal method and catalytically evaluated in CO oxidation. The Co–CeO_2 NR catalyst exhibited optimum low-temperature CO oxidation performance ($T_{50} \approx$ 145 °C) due to its abundance in Ce^{3+} defect sites and active surface oxygen species, along with the high reactivity of the (110) planes existing in ceria nanorods.[44] Furthermore, ceria-based catalysts modified with transition metals (Mn, Co or Cu) in various molar ratios were prepared through the solution combustion method. It was revealed that the synergism of Ce^{3+}–M^{x+}–Ce^{4+} (M = Mn, Co, Cu) ions on the catalyst surface increases the amount of active oxygen species and enhances the low-temperature CO oxidation activity.[45]

Despite the significant interest in cobalt–ceria catalysts for CO oxidation[6,37,44–55] only a limited number of studies has systematically investigated the combined role of ceria shape and cobalt oxide phase in the oxidation of CO, as revealed in the above discussion. More importantly, no definitive conclusions have been drawn in relation to the distinct role of ceria exposed planes and to this context, the present work aims at bridging this gap by methodically examining the effect of ceria morphology and cobalt oxide phase on the local surface chemistry and ultimately on the CO oxidation performance. In particular, the dual role of CeO_2 shape (nanorods-NR and nanocubes-NC) is investigated, both as active catalysts and as tailored supports for the cobalt oxide (Co_3O_4) phase, with systematic evaluation of their CO oxidation performance. The catalysts were characterized by various techniques such as N_2 physisorption, X-ray diffraction (XRD), scanning and transmission electron microscopy (SEM/TEM), temperature-programmed reduction

(TPR), X-ray photoelectron spectroscopy (XPS), and thermogravimetric analysis (TGA), revealing correlations among ceria morphology, Co–Ce interactions, reducibility, and catalytic activity. Notably, ceria nanorods exhibit enhanced textural and redox properties that enable the formation of highly dispersed Co^{2+} active species through synergistic metal–support interactions, resulting in uniform cobalt dispersion and superior CO oxidation performance. These findings underscore the significance of shape-controlled synthesis in catalyst design, towards the development of efficient CO oxidation catalysts.

Experimental

Materials synthesis

The precursor compounds $Ce(NO_3)_3{\cdot}6H_2O$ (99.5%, Thermo Fisher Scientific, 1 Reagent Lane, Fair Lawn, NJ 07410, USA) and $Co(NO_3)_2{\cdot}6H_2O$ (≥98%, Sigma Aldrich Chemie GmbH, Riedstrasse 2, 89555 Steinheim, Germany) were employed for the preparation of bare ceria and Co/CeO_2 mixed oxides. Also, NaOH (≥98%, penta Chemicals Unlimited, Ing. Petr Švec – penta s.r.o., Radiová 1122/1, 102 00 Prague 10, Czech Republic) and ethanol (Merck KGaA, Frankfurter Strasse 250, Darmstadt 64293, Germany) were used during materials synthesis. Initially, bare ceria nanostructures of rod-like (CeO_2-NR) and cubic (CeO_2-NC) morphology were hydrothermally synthesised, as thoroughly described in a previous work of ours.[14] In brief, appropriate amounts of the $Ce(NO_3)_3{\cdot}6H_2O$ and NaOH aqueous solutions were mixed and kept under stirring for 1 h, with the final slurry being transferred into a Teflon bottle and aged for 24 h at 90 °C for ceria nanorods and at 180 °C for ceria nanocubes. The final solid products were recovered through centrifugation during which they were thoroughly washed with ultrapure water until neutral pH and ethanol. Subsequently, the precipitate was dried at 90 °C for 12 h and finally calcined at 500 °C for 2 h (heating ramp 5 °C min^{-1}).

The Co/CeO_2-NX catalysts where NX stands for NR: nanorods and NC: nanocubes were prepared through the wet impregnation method,[56] employing an aqueous solution of $Co(NO_3)_2{\cdot}6H_2O$, in order to achieve a Co/Ce atomic ratio of 0.25 corresponding to 7.8 wt% of Co loading. Heating under stirring of the obtained suspensions until complete water evaporation occurred, followed by drying at 90 °C for 12 h and final calcination at 500 °C for 2 h (heating ramp 5 °C min^{-1}).

Materials characterization

The prepared samples were characterized using a combination of physicochemical techniques, including N_2 adsorption–desorption analysis, X-ray diffraction (XRD), scanning electron microscopy with energy-dispersive X-ray spectroscopy and transmission electron microscopy (SEM–EDS/TEM), temperature-programmed reduction (H_2-TPR), X-ray photoelectron spectroscopy (XPS), Raman analysis and dynamic thermogravimetric analysis (TGA).

XRD measurements were performed using a PANalytical X'Pert Pro diffractometer equipped with Cu Kα radiation to identify the crystalline phases and estimate average crystallite sizes.

The textural properties of the samples, including specific surface area, pore volume, and pore size distribution, were determined by N_2 adsorption–desorption measurements at −196 °C using the Brunauer–Emmett–Teller (BET) and Barrett–Joyner–Halenda (BJH) methods.

The reducibility of the catalysts was investigated by H_2-TPR experiments, while the surface morphology, particle size, and elemental distributions were examined by SEM and TEM coupled with energy-dispersive X-ray spectroscopy (EDS) system.

Raman analysis was conducted in order to gain insight into the structural properties and the cobalt distribution of the cobalt–ceria samples.

XPS analysis was employed to determine the surface chemical composition and oxidation states of cerium, cobalt, and oxygen species.

Dynamic thermogravimetric analysis was conducted under CO/O_2 containing atmospheres to probe oxygen release behaviour under reaction-relevant conditions.

Detailed experimental procedures, instrumental parameters, and data analysis methodologies for all characterization techniques are provided in the SI.

Catalytic evaluation studies

Catalytic tests for CO oxidation were carried out in a quartz fixed-bed reactor (8 mm i.d.), loaded with 100 mg of catalyst. The total flow rate of the feed gas (2000 ppm CO and 1.0 vol% O_2 in He) was 250 cm^3 min^{-1}, corresponding to a gas hour space velocity (GHSV) of 60 000 h^{-1}. Catalytic evaluation measurements were carried out by increasing the temperature by 20 degrees steps up to 550 °C. The reactant CO was analysed by using a CO analyser (AO2000, ABB Automation GmbH, Stierstädter Strasse 5, 60488 Frankfurt, Germany). The conversion of CO (X_{CO}, %) was calculated by the following equation (eqn (1)):

$$X_{CO}\,(\%) = \frac{[CO]_{in} - [CO]_{out}}{[CO]_{in}} \times 100 \quad (1)$$

where $[CO]_{in}$ and $[CO]_{out}$ are the CO concentration (ppm) in the inlet and outlet gas streams, respectively.

Results and discussion

Catalytic evaluation studies: CO oxidation

The bare ceria catalysts and the cobalt–ceria ones were catalytically evaluated in the oxidation of CO. Fig. 1 exhibits the conversion of CO as a function of temperature for bare ceria and Co/CeO_2 samples. In particular, in terms of half-conversion temperature (T_{50}), the following order is obtained: Co/CeO_2-NR (127 °C) < Co/CeO_2-NC (143 °C) < CeO_2-NR (310 °C) < CeO_2-NC (371 °C). The addition of cobalt into the ceria supports greatly enhances the catalytic activity, with the rod-shaped Co/CeO_2 sample exhibiting the optimum performance, offering a complete CO elimination at a very

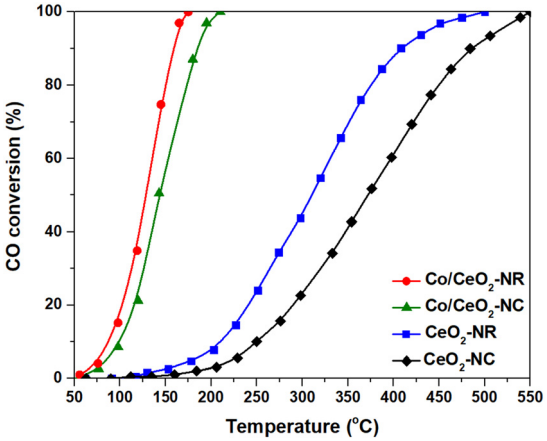

Fig. 1 CO conversion as a function of temperature for bare CeO_2 and Co/CeO_2 samples of rod-like (NR) and cubic (NC) morphology. Reaction conditions: 2000 ppm CO, 1 vol% O_2, GHSV = 60 000 h^{-1}.

low temperature (164 °C). In addition, the specific activity, normalized per unit of catalyst mass (nmol g^{-1} s^{-1}) was calculated at differential conditions (X_{CO} < 20%, T = 100 °C, GHSV = 60 000 h^{-1}), as the intrinsic reactivity of the as-prepared catalysts can be more precisely reflected. In particular, in terms of specific activity the Co/CeO_2-NC and Co/CeO_2-NR samples exhibit 326 and 581 nmol g^{-1} s^{-1}, respectively.

Apparently, the rod-shaped Co/CeO_2-NR catalyst exhibits the optimum catalytic performance, in terms of both conversion and specific activity. It should be also mentioned that the optimum catalyst (Co/CeO_2-NR) exhibited a stable conversion performance in short-term stability tests (24 h).

The main textural characteristics of bare ceria samples and Co/CeO_2 mixed oxides are summarized in Table 1. Bare ceria supports exhibit higher BET surface areas than their corresponding mixed oxides, with CeO_2-NR showing a substantially larger surface area (68.4 m^2 g^{-1}) compared to CeO_2-NC (23.9 m^2 g^{-1}).

The addition of cobalt into the ceria carriers leads to a decrease in the surface area ranging between 14 and 19%, as similarly observed in copper–ceria catalysts of different morphology (nanorods, nanopolyhedra, nanocubes),[14] yielding the following order: CeO_2-NR (68.4 m^2 g^{-1}) > Co/CeO_2-NR (55.6 m^2 g^{-1}) > CeO_2-NC (23.9 m^2 g^{-1}) > Co/CeO_2-NC (20.6 m^2 g^{-1}).

Textural and structural analysis (BET and XRD)

Fig. 2a presents the adsorption–desorption isotherms for the CeO_2 and Co/CeO_2 samples of different morphology. All the samples exhibit type IV isotherms with a hysteresis loop at a relative pressure >0.5, indicating their mesoporous nature.[57] In Fig. 2b, the Barrett–Joyner–Halenda (BJH) desorption pore size distributions (PSD) of bare ceria and Co/CeO_2 catalysts are shown. All the samples present a wide PSD while exhibiting maxima at pore diameters larger than 3 nm, corroborating the mesoporosity of the catalysts. Regarding the average pore diameter, the following order is obtained: CeO_2-NC (31.5 nm) > Co/CeO_2-NC (28.1 nm) > CeO_2-NR (24.3 nm) > Co/CeO_2-NR (18.7 nm).

X-ray diffraction (XRD) was employed to analyse the crystal structure of both bare ceria supports and cobalt-supported ceria with various morphologies. The corresponding diffraction patterns are presented in Fig. 3a and b, respectively. All XRD profiles exhibit the characteristic reflections of the fluorite-type CeO_2 structure (space group *Fm3m*), with prominent peaks appearing at 28.7°, 33.1°, 47.6°, and 56.5°, corresponding to the (111), (200), (220), and (311) planes, respectively.[58] The addition of Co into CeO_2-NR/NC resulted in additional diffraction peaks in the XRD patterns of Co/CeO_2-NC and Co/CeO_2-NR. Notably, peaks observed at 2θ = 37.1° and 65.5° correspond to the (311) and (440) planes of Co_3O_4, respectively.[59] These findings indicate that both Co/CeO_2-NR and Co/CeO_2-NC samples contain a combination of the face-centred cubic fluorite phase of ceria and the cubic spinel structure of Co_3O_4.

In addition to identifying the crystal phases, the average crystallite size (D_{XRD}) of the as-prepared samples was calculated using the Scherrer equation (eqn (S1) in SI), based on the full width at half maximum (FWHM) of the most intense diffraction peaks. The results are summarized in Table 1. The average crystallite sizes for CeO_2-NC and CeO_2-NR are approximately 17 nm and 15 nm, respectively. Upon cobalt addition, the average crystallite size of CeO_2 increases to 28 nm in Co/CeO_2-NC and slightly decreases to 12 nm in Co/CeO_2-NR, indicating morphology-dependent crystallite growth behaviour. Similarly, the crystallite size of the Co_3O_4 phase is calculated to be 22 nm for Co/CeO_2-NC and 18 nm for Co/CeO_2-NR. It is obvious that cobalt addition in ceria nanorods (NR) does not affect the ceria crystallite size, whereas in nanocubes (NC), the ceria crystallite size is

Table 1 Textural and structural properties of bare CeO_2 and Co/CeO_2 samples of different morphology

	BET analysis			XRD analysis		
				Average crystallite size, D_{XRD} (nm)		Lattice parameters (nm)
Sample	BET surface area (m^2 g^{-1})	Pore volume (cm^3 g^{-1})	Average pore diameter (nm)	CeO_2(111)	Co_3O_4(113)	$a = b = c$
CeO_2-NC	23.9	0.19	31.5	17	—	0.538
CeO_2-NR	68.4	0.41	24.3	15	—	0.538
Co/CeO_2-NC	20.6	0.14	28.1	28	22	0.537
Co/CeO_2-NR	55.6	0.26	18.7	12	18	0.534

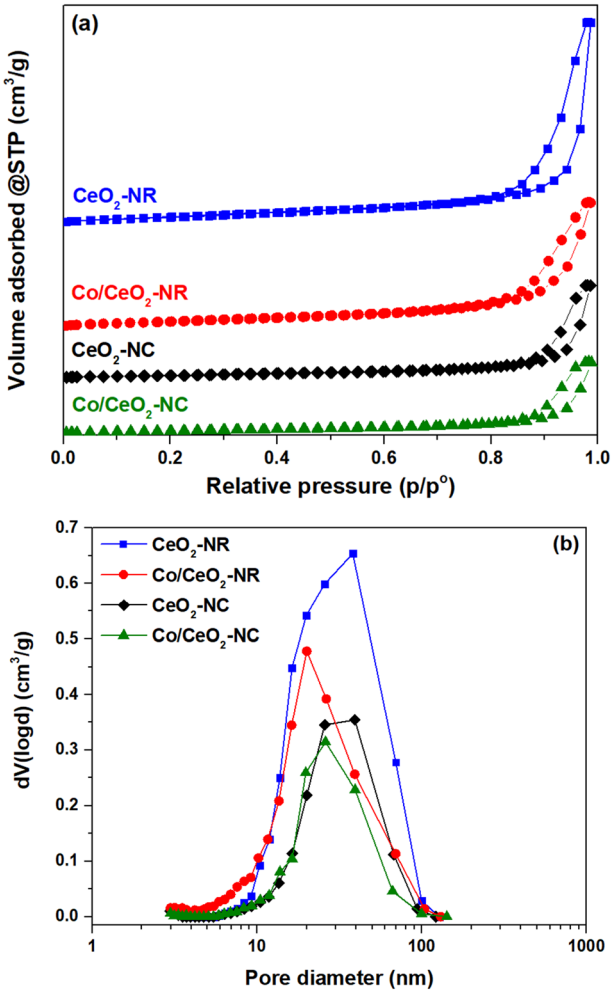

Fig. 2 (a) The adsorption–desorption isotherms and (b) the BJH (Barrett–Joyner–Halenda) desorption pore size distribution (PSD) of CeO_2 and Co/CeO_2 samples of different morphology.

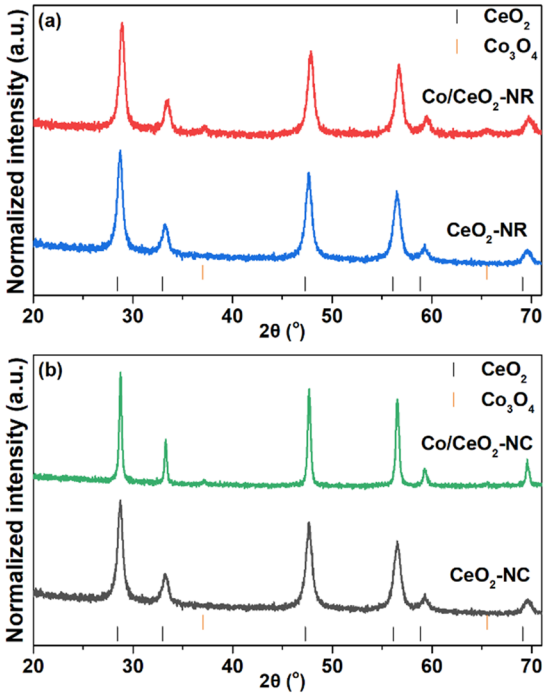

Fig. 3 XRD patterns of (a) CeO_2-NR and Co/CeO_2-NR, (b) CeO_2-NC and Co/CeO_2-NC samples of different morphology.

significantly increased. After Co impregnation, the samples of nanocubic morphology (NC) become more prone to sintering. This can be well interpreted by taking into consideration the distinct surface chemistries of the exposed ceria facets. In particular, for cube-like nanoparticles, the perfect cubic structure is rarely reported in the literature; instead, nanocubes typically display rounded corners and edges, revealing {111} and {110} facets, respectively.[12] Under these conditions and as revealed by TEM analysis (*vide infra*), the impregnated cobalt species tend to segregate and get preferentially localised at the edges and corners of nanocubes. The accumulation of these CoO_x domains at high-energy corners and edges may promote localised surface diffusion and particle coalescence during calcination, resulting in an increase in the measured crystallite size. In contrast, ceria nanorods predominantly expose the more reducible {110} and {100} facets, where oxygen vacancies form more readily, as demonstrated in our previous work using *in situ* Raman spectroscopy.[14] These vacancies allow cobalt to strongly anchor to the support, resulting in a uniform distribution over the entire surface of the nanorods, as confirmed by TEM analysis. Such interactions stabilise defect-rich ceria domains, suppress sintering, and introduce microstrain, manifesting as an apparent decrease in the crystallite size. Hence, the opposite effects of cobalt addition arise from the facet-dependent interplay between cobalt species, oxygen vacancies, and the sintering behaviour of CeO_2, as further discussed below.

Additionally, a slight decrease in the lattice parameter was observed upon cobalt addition. The lattice constant of nano CeO_2 (a = 0.538 nm) is marginally reduced to 0.537 nm in Co/CeO_2-NC and further to 0.534 nm in Co/CeO_2-NR. This reduction in lattice parameter indicates that a small fraction of $Co^{2+/3+}$ ions may be incorporated into the CeO_2 fluorite lattice. Given that the ionic radii of Co^{2+} (0.074 nm) and Co^{3+} (0.061 nm) are significantly smaller than that of Ce^{4+} (0.097 nm),[60] their substitution into the lattice leads to unit cell shrinkage, shifting the XRD peaks to higher 2θ values.

Morphological (SEM and TEM) and structural (Raman) analysis

To investigate the influence of ceria morphology on the catalyst structure, the as-prepared samples were analysed by electron microscopy. Fig. 4 provides a detailed morphological analysis of the nanorod-based catalysts (CeO_2-NR and Co/CeO_2-NR). Fig. 4a–d displays the morphology of the bare CeO_2-NR support. SEM image in Fig. 4a shows that the material consists of a large, interconnected network of

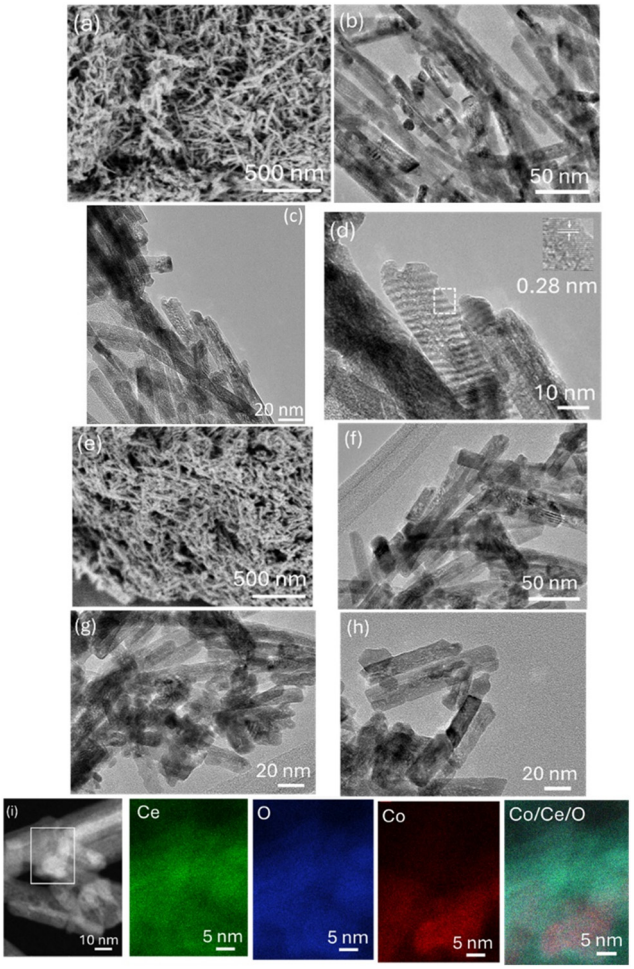

Fig. 4 SEM and HRTEM images of CeO_2-NR (a–d) and Co/CeO_2-NR (e–h), (i) HAADF-STEM spectra and corresponding EDS elemental mapping of Co/CeO_2-NR. The inset in Fig. 4d shows a magnification of the lattice fringes.

uniform, rod-shaped nanostructures. The HR-TEM images in Fig. 4b and c provide a view at increasing magnification, confirming the rod-like morphology of CeO_2 with a mean width of about 15 nm and a length varied from 30 to 200 nm. Fig. 4d reveals the crystalline nature of the CeO_2-NR. Clear lattice fringes are visible, and the measured interplanar spacing of 0.28 nm is consistent with the (200) crystallographic plane of the fluorite-type CeO_2 structure.[61] This confirms the successful synthesis of crystalline ceria with a controlled nanorod shape. Fig. 4e–h characterises the Co/CeO_2-NR catalyst after the incorporation of cobalt *via* the wet impregnation method. The SEM image in Fig. 4e shows that the overall morphology of the support is well preserved after the addition of cobalt. The HR-TEM images in Fig. 4f–h provide a closer look at the catalyst. It can be observed that smaller nanoparticles with an average size of 7–12 nm, which appear with a darker contrast, are dispersed on the surface of CeO_2-NR. To identify these particles, high-angle annular dark-field scanning transmission electron microscopy (HAADF-STEM) image and corresponding EDS elemental maps analysis was done.

The EDS maps in Fig. 4i clearly show the spatial distribution of Ce (green), O (blue) and Co (red) elements. The Ce and O maps perfectly outline the nanorod structure, as expected. Crucially, the Co map shows that cobalt is well-dispersed as nanoclusters across the surface of the ceria nanorod. These nanoclusters are identified as cobalt oxide, which is consistent with the XRD findings that show the presence of both CeO_2 and Co_3O_4 crystal phases. The overlay image of Ce, Co and O EDS maps confirms the intimate contact between the cobalt oxide particles and the ceria support.

Fig. 5 presents the morphological analysis of the nanocube-based catalysts (CeO_2-NC and Co/CeO_2-NC). Fig. 5a and d displays the morphology of the bare CeO_2-NC support. While the precise morphology of the CeO_2-NC sample is difficult to discern from the SEM image (Fig. 5a) due to poor magnification, subsequent analysis by HR-TEM unequivocally confirms the material's well-defined nanocubic shape (Fig. 5b–d). Fig. 5d also shows visible lattice fringes and has a measured spacing of 0.30 nm, which corresponds well with the (111) plane of the CeO_2 crystal structure.[61] This observation is consistent with the literature, which states that

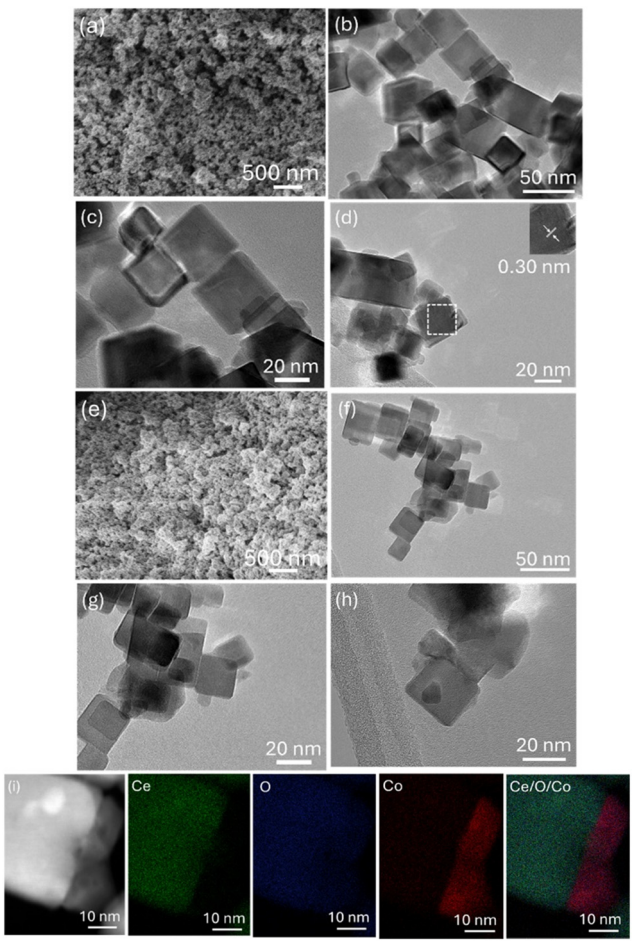

Fig. 5 SEM and HRTEM images of CeO_2-NC (a–d) and Co/CeO_2-NC (e–h), (i) HAADF-STEM spectra and corresponding EDS elemental mapping of Co/CeO_2-NC. The inset in Fig. 5d shows a magnification of the lattice fringes.

ceria nanocubes and polyhedra tend to expose the stable {111} facets.[12]

It is worth noting that a perfect cubic morphology of CeO_2 is rarely achieved;[12,62] instead, ceria nanocubes typically exhibit rounded corners and edges that expose the more stable {111} and {110} facets. In line with this, Fig. 5d shows clear lattice fringes with a measured spacing of 0.30 nm, which can be assigned to the (111) plane of CeO_2, confirming that the nanocubes predominantly expose {111} facets.[12,62]

Fig. 5e–h shows that the cubic morphology of the CeO_2 support is perfectly maintained after the wet impregnation of cobalt. To determine the cobalt oxide distribution, STEM EDS analysis was performed on the Co/CeO_2 NC sample (Fig. 5i). The EDS elemental maps provide critical insight into the composition. The maps for O (blue) and Ce (green) perfectly align with the cubic shape, confirming the identity of the support. Most notably, the map for Co (red) reveals that the cobalt is not uniformly distributed. Instead, it appears to be preferentially concentrated along the edges and corners of the CeO_2 nanocube with an average size of 7–15 nm. The overlay image of Ce, O and Co confirms this site-specific deposition, showing the cobalt oxide nanoparticles decorating the edges of the ceria nanocube. This contrasts with Co/CeO_2-NR catalyst, where cobalt oxide was found to be highly dispersed as nanoclusters across the surface of the nanorods. This variation in Co_3O_4 distribution, dictated by the support shape and facets, provides a structural basis for the different Co–Ce interactions and facet-dependent crystallite growth.

Raman spectroscopy (Fig. 6) was employed to assess the structural properties and spatial distribution of the supported cobalt species on the ceria nanorods (Co/CeO_2-NR) and nanocubes (Co/CeO_2-NC). All spectra exhibit a sharp, prominent peak at ~464 cm^{-1}, which corresponds to the symmetric stretching F_{2g} mode characteristic of the fluorite CeO_2 lattice.[14,63–66] Additionally, distinct peaks observed at ~482, 522, 618, and a highly intense peak at ~691 cm^{-1} are assigned to the vibrational modes of the spinel Co_3O_4 phase.[66–69] The strong intrinsic Raman scattering of the highly active Co_3O_4 phase overlaps and heavily masks the 550–600 cm^{-1} region where the defect-induced (D) band of CeO_2 typically appears.

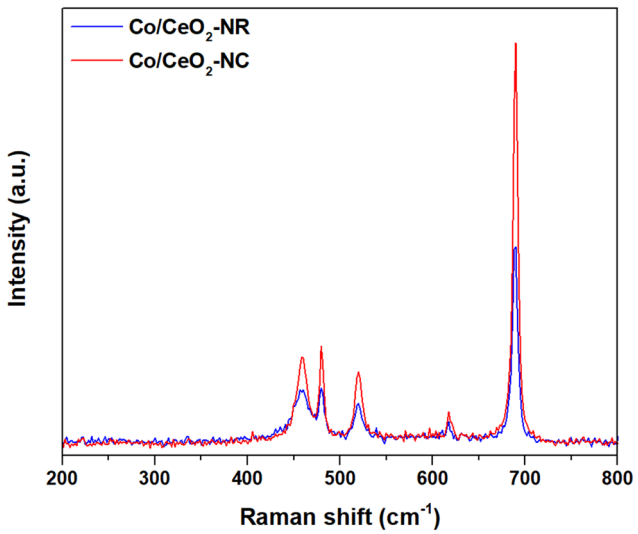

Fig. 6 Raman spectra for cobalt–ceria catalysts of different morphologies (NR-nanorods and NC-nanocubes).

A comparative analysis of the peak intensities provides significant insight into the dispersion of the cobalt phase, corroborating the morphological observations (Fig. 4 and 5). Multi-point analysis (see SI) across the samples reveals pronounced spatial heterogeneity, with the Co/CeO_2-NC sample displaying notably higher intensity ratios of the Co_3O_4 modes relative to the CeO_2 support. Such elevated relative intensities of the metal oxide phase indicate localized agglomeration and larger crystallite sizes, which yield a stronger bulk Raman scattering signal.[70,71] Conversely, the Co/CeO_2-NR sample exhibits systematically lower relative Co_3O_4 intensities, characteristic of a highly dispersed cobalt phase. These spectroscopic findings are in excellent agreement with the TEM results, verifying that cobalt is highly dispersed across the surface of the ceria nanorods, whereas it preferentially agglomerates into larger clusters at the edges and corners of the ceria nanocubes.

Reducibility studies (H_2-TPR) and thermogravimetric analysis (TGA)

Fig. 7a shows the TPR profiles of bare ceria supports which consist of two wide peaks at 526–551 °C and at temperatures higher than 800 °C. These peaks can be attributed to ceria surface (O_s) and bulk (O_b) oxygen reduction, respectively.[72,73] Table 2 presents the hydrogen consumption of the samples. On the basis of surface-to-bulk oxygen ratio (O_s/O_b), ceria nanorods exhibit a much higher ratio (0.96) than ceria nanocubes (0.41), indicating their abundance in loosely bound oxygen species.

The reduction profiles of the Co/CeO_2 samples, as well as of a commercial Co_3O_4 reference sample are presented in Fig. 7b. Commercial Co_3O_4 shows a small shoulder peak at 360 °C attributed to the reduction of Co_3O_4 to CoO and a large peak at 477 °C which corresponds to the CoO to metallic cobalt reduction.[37,56]

The Co/CeO_2 samples of different morphology exhibit four reduction peaks. Probably, peak a is ascribed to the reduction of adsorbed reactive oxygen species which originate from the formation of a solid solution Co–O–Ce.[74] The formation of this phase is directly corroborated by the structural analysis (Fig. 3), which revealed a significant contraction of the ceria lattice parameter due to cobalt ion insertion. Peaks b and c correspond to the reductions of Co^{3+} to Co^{2+} and of Co^{2+} to Co^0, respectively.[72,75,76] Moreover, the Co/CeO_2 samples show a wide peak at temperatures above 800 °C, which is ascribed to the ceria sub-surface oxygen reduction.[72,77,78] Evidently, the reduction of Co/CeO_2 mixed oxides takes place at lower

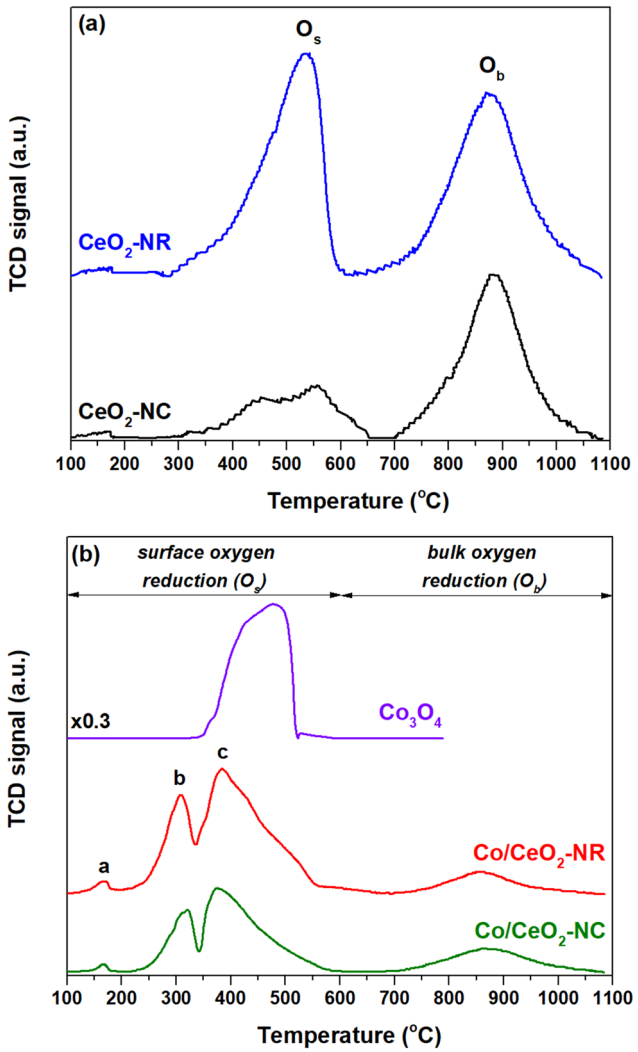

Fig. 7 H_2-TPR profiles of (a) bare CeO_2 and (b) commercial Co_3O_4 and Co/CeO_2 samples.

Table 2 Redox properties of bare CeO_2, commercial Co_3O_4 and Co/CeO_2 samples

	H_2 consumption[a] (mmol H_2 per g_{cat})			
Sample	O_s	O_b	Total	O_s/O_b
CeO_2-NR	0.51	0.53	1.04	0.96
CeO_2-NC	0.17	0.41	0.58	0.41
Co/CeO_2-NR	2.73	0.42	3.15	6.5
Co/CeO_2-NC	1.58	0.49	2.07	3.22
Co_3O_4 (commercial)	—	—	17.6	—

[a] Estimated by the area of the corresponding TPR peaks at temperatures $T < 600$ °C (O_s) and $T > 600$ °C (O_b), calibrated against a known amount of CuO standard sample.

temperatures in comparison to the bare ceria supports, indicating the key role of Co in the ceria surface oxygen reduction. The Co–ceria interaction could be accounted for the enhanced reducibility and oxygen mobility, as evidenced in previous studies.[14,79]

These observations are consistent with the thermogravimetric profiles of the CeO_2 and Co/CeO_2 samples shown in Fig. 8. CeO_2-NR exhibits more pronounced weight loss compared to CeO_2-NC, reflecting its superior oxygen-exchange kinetics. The addition of Co markedly increases the overall weight loss in both nanocubic and nanorod systems, reflecting the enhanced reducibility induced by cobalt. Specifically, the Co/CeO_2-NR sample exhibits the highest mass loss (~2%), whereas Co/CeO_2-NC shows a more modest decrease (~0.8%). This difference, roughly a factor of 2.5, indicates that the nanorod morphology provides significantly more labile oxygen species accessible within the low-temperature range where catalytic activity is observed (Fig. 8b). Notably, when these mass losses are expressed as oxygen removed per catalyst mass, the contrast becomes even clearer. The Co/CeO_2-NR sample releases approximately 1.25 mmol of oxygen per gram of catalyst, while the Co/CeO_2-NC sample releases only about 0.5 mmol of oxygen per gram of catalyst. Such a difference demonstrates that the nanorod structure, in combination with Co addition, supports much

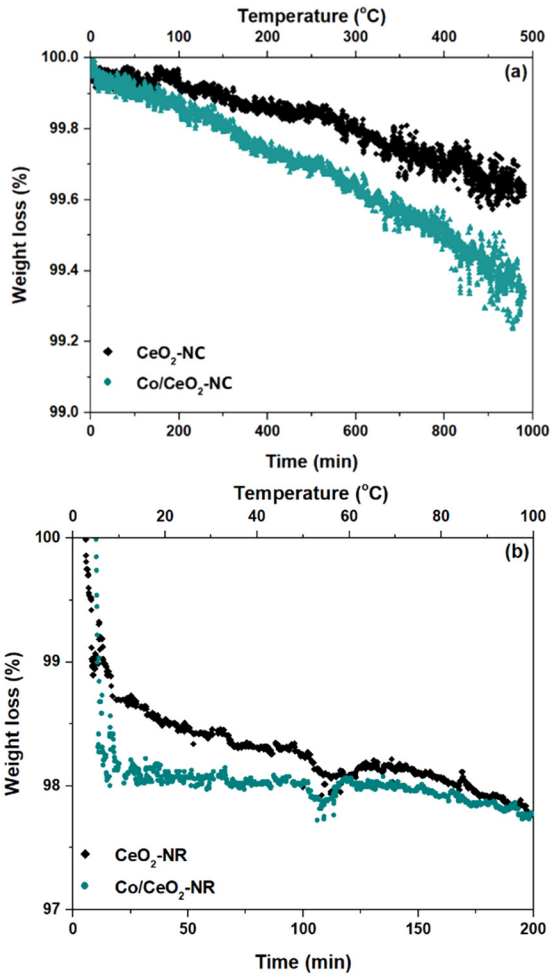

Fig. 8 Thermogravimetric curves of (a) CeO_2-NC and Co/CeO_2-NC, (b) CeO_2-NR and Co/CeO_2-NR.

more extensive oxygen vacancy formation and oxygen mobility than the cube structure. This enhanced low-temperature oxygen availability provides a direct explanation for the superior redox behaviour (Fig. 7) and typically superior catalytic performance (Fig. 1) of the Co-modified nanorod system.

In Table 2, the hydrogen consumption of the samples, as well as of the commercial one is presented. The Co/CeO_2-NR sample exhibits the highest H_2 consumption (3.15 mmol H_2 per g_{cat}) and a surface-to-bulk oxygen ratio of 6.5, twice the corresponding value for the Co/CeO_2-NC sample of cubic morphology, revealing once more the significance of ceria shape in the reducibility of the materials. The present findings closely corroborate our previous results – obtained *via in situ* Raman[14] and transient isotopic[80] studies – regarding the impact of ceria morphology on structural defects and oxygen-exchange kinetics. Specifically, ceria nanorods exhibit a higher abundance of oxygen vacancies compared to nanocubes. This, in turn, lowers the activation energy barrier for surface oxygen reduction and bulk oxygen diffusion,[80] leading to superior catalytic performance in oxidation and reduction processes where oxygen replenishment and mobility play a pivotal role.

Surface analysis (XPS)

The surface properties of the materials were also characterised by XPS for both NR and NC samples. The binding energy (BE) correction was conducted by the alignment of the C 1s peak for each material. A detailed analysis of the Ce 3d and Co 2p spectra, including fitted peaks and their corresponding assignments, is provided in the SI. XPS analysis confirmed the presence of multiple cobalt oxidation states (Co^{2+}/Co^{3+}) across all cobalt–ceria catalysts, together with mixed Ce^{3+}/Ce^{4+} species in the ceria phase, indicating the coexistence of reduced and oxidised surface states. Quantitative analysis of the Co 2p spectra revealed that the Co/CeO_2-NR sample exhibits a higher surface Co^{2+}/Co^{3+} ratio (≈2.15) compared to Co/CeO_2-NC (≈1.93), suggesting a greater abundance of active Co^{2+} sites on the rod-shaped catalyst (Table 3).

The analysis of the Ce 3d spectra reveals a clear dependence of the cerium oxidation state on both the support morphology and the presence of the cobalt phase. For the bare supports, the CeO_2-NR sample exhibits a notably higher Ce^{3+}/Ce^{4+} ratio (0.43) compared to CeO_2-NC (0.35). This indicates a higher abundance of surface oxygen vacancies in the nanorods, as previously elaborated. However, upon cobalt impregnation, the Ce^{3+} concentration decreases significantly – especially in the case of Co/CeO_2-NR – levelling off at a ratio of *ca.* 0.28. This drop probably suggests a strong interaction between the cobalt species and the support, involving a redox equilibrium where Ce^{3+} sites are consumed to stabilize the dispersed cobalt phase (Co^{2+}/Co^{3+} and Ce^{4+}/Ce^{3+} redox equilibrium), as reported for ceria-based transition metal catalysts.[14]

Table 3 Surface properties of bare CeO_2 and Co/CeO_2 samples of different morphology

Sample	Ce^{3+} (at%)	Ce^{4+} (at%)	Ce^{3+}/Ce^{4+}	Co^{2+}/Co^{3+}	O_I/O_{II}
CeO_2-NR	29.98	70.02	0.43	—	2.07
CeO_2-NC	26.02	73.98	0.35	—	2.06
Co/CeO_2-NR	22	78	0.28	2.15	1.08
Co/CeO_2-NC	21.88	78.12	0.28	1.93	0.89

The O 1s spectra (Fig. 9) were deconvoluted into two principal components in all samples, with an additional third component observed for the nanocubic (NC) samples. The main peak (O_I, ~529 eV) is assigned to lattice oxygen (O^{2-}) in the CeO_2 lattice, while the secondary peak (O_{II}, ~531 eV) corresponds to surface/loosely bound oxygen species (O^-, O_2^{2-}), adsorbed hydroxyls, water and carbonate-related species.[14] The O_I component is primarily associated with oxygen coordinated to Ce^{4+}, whereas the O_{II} component corresponds to defect-rich oxygen species, such as adsorbed hydroxyls and carbonates.[81] For the NC samples an additional O_{III} peak at ~533 eV is present and is attributed to weakly adsorbed molecular oxygen and physisorbed water.[81,82] The measured O_I/O_{II} ratios follow the order CeO_2-NR (2.07) > CeO_2-NC (2.06) > Co/CeO_2-NR (1.08) > Co/CeO_2-NC (0.89), indicating that the bare nanorods contain the highest fraction of lattice oxygen relative to loosely bound surface oxygen, and that cobalt incorporation increases the relative abundance of surface/adsorbed oxygen species.

The results of the present study regarding the oxidation of CO over ceria-based catalysts can be well rationalised within the framework of a Mars–van Krevelen redox-type mechanism. According to this mechanistic scheme,[48,82–84] the CO molecule is chemisorbed on the Co^{2+} active sites and the chemisorbed CO migrates to the metal–support interface. Then, molecular oxygen is activated on ceria oxygen vacancies towards the formation of active oxygen species which react with the chemisorbed CO at the interface. Moreover, the Co^{2+} sites are regenerated and the oxygen vacancies are refilled by gas phase oxygen through consecutive catalytic cycles. Taking into account the above mechanism, the reducibility of ceria carrier and its interaction with the cobalt species become highly relevant. More specifically, ceria nanorods exhibit enhanced reducibility and oxygen mobility,[14,80] thus enabling active oxygen species formation, while the synergistic cobalt–ceria interactions, also favoured by the high dispersion of cobalt over the entire surface of ceria nanorods, as corroborated by SEM–EDS and Raman analysis, can be accounted for the abundance of active Co^{2+} species in the rod-shaped sample and its superior catalytic activity.

The CO oxidation performance of bare ceria and Co–ceria samples totally coincides, showcasing the fundamental role of ceria carrier (Fig. 1). Nevertheless, the mixed oxides are superior to the bare ones due to the synergistic metal–support interactions, as revealed by their enhanced reducibility, in terms of both TPR onset temperature and hydrogen consumption (Table 2 and Fig. 7). In light of the

above discussion, Fig. 10 illustrates the correlations between the surface-to-bulk oxygen ratio (O_s/O_b, reflecting the abundance of labile oxygen species), the Co^{2+}/Co^{3+} ratio (representing the fraction of active cobalt sites), the O_I/O_{II} ratio (indicating the fraction of lattice oxygen), and the oxygen loss per catalyst mass (indicative of oxygen species abundance) with the specific reaction rates of Co/CeO_2 catalysts with cubic and rod-like morphologies. The Co/CeO_2-NR exhibits high cobalt dispersion and the highest surface-to-bulk ratio leading to improved reducibility. Its abundance in loosely bound oxygen species plays a pivotal role in active oxygen species formation and consequently in the CO oxidation reaction. On the basis of the present data, the enhanced activity of Co/Ceria nanorods is attributed to the unique surface architecture of the nanorods, which simultaneously provides active oxygen sites and maximizes the efficiency of the cobalt active phase through superior dispersion.

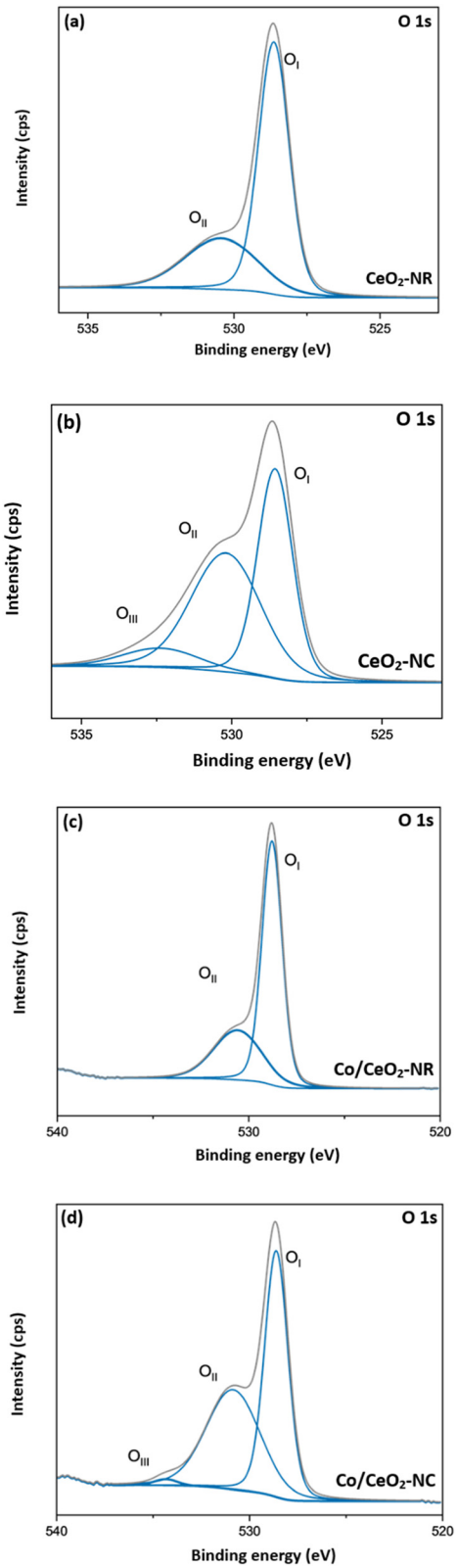

Fig. 9 O 1s XPS spectra of (a) CeO_2-NR, (b) CeO_2-NC, (c) Co/CeO_2-NR and (d) Co/CeO_2-NC.

Conclusions

Ceria nanorods (NR) and nanocubes (NC) with different crystal facets were hydrothermally synthesised and used as supports for the cobalt oxide phase which was introduced through the wet impregnation method. The oxidation of CO was employed as a probe reaction to gain insight into the ceria shape effects on the structural, redox, surface properties, and consequently on the catalytic performance. In terms of half-conversion (T_{50}) temperature and specific activity, cobalt–ceria nanorods were superior to nanocubes, offering complete CO elimination at 164 °C. The results clearly revealed the significance of ceria morphology on the reducibility and active oxygen species formation, with the Co/ceria-NR catalyst exhibiting high cobalt dispersion throughout the entire surface of ceria nanorods, and abundance in weakly bound oxygen species and partially reduced Co^{2+} species, with the latter being considered as the

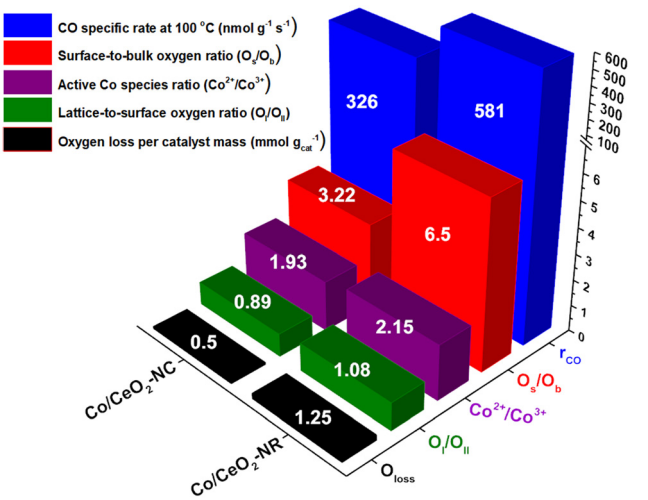

Fig. 10 Relationships of the CO specific rate at 100 °C with the surface-to-bulk oxygen ratio (O_s/O_b) derived by TPR, the Co^{2+}/Co^{3+} and O_I/O_{II} ratios derived by XPS and the amount of oxygen loss derived by dynamic TGA for the Co/CeO_2 catalysts of different morphology (NR-nanorods, NC-nanocubes).

active centres for the CO oxidation reaction. The present findings are substantiated by the structure–activity relationships of the CO specific rate with the surface-to-bulk oxygen ratio (O_s/O_b), the Co^{2+}/Co^{3+} and O_I/O_{II} ratios, and the amount of oxygen loss per catalyst mass for the cobalt–ceria nanocubes and nanorods.

Even though the superior catalytic performance of the nanorods is evident, disentangling the specific contribution of the reactive crystal facets from the improved cobalt dispersion remains a challenge, as these factors are intrinsically coupled; the defect-rich surfaces naturally promote stronger metal–support interactions and higher dispersion. To fully decouple these effects, future studies involving rationally designed experiments – such as the deposition of size-controlled cobalt nanoparticles onto ceria nanoparticles of specific morphologies or the use of single-atom catalysts – would be of great interest to isolate the role of surface termination from particle size effects.

Author contributions

A. O. and M. L. contributed to materials synthesis and characterisation (BET and H_2-TPR), catalytic evaluation, results interpretation and paper writing. A. K. B., S. S. and K. K. contributed to materials characterisation (XRD, SEM, TEM, XPS) and results interpretation. G. D., G. A. M. and E. I. P. contributed to materials characterization (TGA, Raman) and results interpretation. M. K. contributed to the conception, design, results interpretation and writing of the paper. All authors contributed to the discussion, read and approved the final version of the manuscript.

Conflicts of interest

There are no conflicts to declare.

Data availability

Data for this article, including the materials characterisation results, catalytic evaluation studies and structure–activity correlations, are available at the University of Surrey repository: https://doi.org/10.15126/surreydata.901908.

Supplementary information (SI) is available. See DOI: https://doi.org/10.1039/d5cy01612f.

Acknowledgements

K. K. would like to acknowledge funding *via* the Engineering and Physical Science Research Council (EP/Y015487/1).

References

1 Growth in global energy demand surged in 2024 to almost twice its recent average – News – IEA, https://www.iea.org/news/growth-in-global-energy-demand-surged-in-2024-to-almost-twice-its-recent-average, (accessed 27 May 2025).
2 J. He, X. Yang, Z. Zhu, X. Luo, C. E. Wu, Y. Cui, Q. Ge, J. Qiu, L. Xu and M. Chen, *Ceram. Int.*, 2024, **50**, 36363.
3 N. K. Soliman, *J. Mater. Sci. Technol.*, 2019, **8**, 2395.
4 M. Konsolakis, *Appl. Catal., B*, 2016, **198**, 49.
5 H. He, P. Yang, J. Li, R. Shi, L. Chen, A. Zhang and Y. Zhu, *Ceram. Int.*, 2016, **42**, 7810.
6 S. A. Mock, S. E. Sharp, T. R. Stoner, M. J. Radetic, E. T. Zell and R. Wang, *J. Colloid Interface Sci.*, 2016, **466**, 261.
7 M. Lykaki, E. Pachatouridou, E. Iliopoulou, S. A. C. Carabineiro and M. Konsolakis, *RSC Adv.*, 2017, **7**, 6160.
8 M. Konsolakis and M. Lykaki, *Catalysts*, 2020, **10**, 160.
9 H. Wu and L. Wang, *Catal. Commun.*, 2011, **12**, 1374.
10 S. Hirabayashi and M. Ichihashi, *J. Phys. Chem. A*, 2013, **117**, 9005.
11 S. Liu, Y. Xue, Y. Jia, H. Wang, Q. Nie and J. Fan, *Sep. Purif. Technol.*, 2024, **359**, 130556.
12 A. Trovarelli and J. Llorca, *ACS Catal.*, 2017, **7**, 4716.
13 J. Chen, M. Jiang, J. Chen, W. Xu and H. Jia, *J. Hazard. Mater.*, 2020, **392**, 122511.
14 M. Lykaki, E. Pachatouridou, S. A. C. Carabineiro, E. Iliopoulou, C. Andriopoulou, N. Kallithrakas-Kontos, S. Boghosian and M. Konsolakis, *Appl. Catal., B*, 2018, **230**, 18.
15 H. E. Rudel, M. K. M. Lane, C. L. Muhich and J. B. Zimmerman, *ACS Nano*, 2020, **14**, 16472.
16 K. Wu, L. D. Sun and C. H. Yan, *Adv. Energy Mater.*, 2016, **6**, 1600501.
17 L. Dong, X. Yao and Y. Chen, *Chin. J. Catal.*, 2013, **34**, 851.
18 C. J. Pan, M. C. Tsai, W. N. Su, J. Rick, N. G. Akalework, A. K. Agegnehu, S. Y. Cheng and B. J. Hwang, *J. Taiwan Inst. Chem. Eng.*, 2017, **74**, 154.
19 B. Yang, X. Chen, L. Guo and L. Zhang, *J. Mater. Chem. A*, 2024, **12**, 19861.
20 T. Wang, J. Hu, R. Ouyang, Y. Wang, Y. Huang, S. Hu and W. X. Li, *Science*, 2024, **386**, 915.
21 H. Wang, Z. Gao, B. Sun, S. Mu, F. Dang, X. Guo, D. Ma and C. Shi, *Chem Catal.*, 2023, **3**, 100768.
22 W. Yang, X. Wang, S. Song and H. Zhang, *Chem*, 2019, **5**, 1743–1774.
23 W. Van Hoey, A. Rokicinska, M. Debosz, I. Majewska, P. Kustrowski and P. Cool, *Mater. Adv.*, 2024, **5**, 6983.
24 J. Jansson, M. Skoglundh, E. Fridell and P. Thormählen, *J. Catal.*, 2002, **211**, 387.
25 G. A. H. Mekhemer, A. I. M. Rabee, C. B. A. Gaid and M. I. Zaki, *Colloids Surf., A*, 2023, **663**, 130992.
26 L. Zhong, M. Barreau, V. Caps, V. Papaefthimiou, M. Haevecker, D. Teschner, W. Baaziz, E. Borfecchia, L. Braglia and S. Zafeiratos, *ACS Catal.*, 2021, **11**, 5369.
27 A. Banerjee, H. Dai, J. Wang, P. Da Costa, M. I. Fadlalla, T. M. Nyathi and M. Claeys, *Catalysts*, 2022, **12**, 118.
28 L. Zhong, T. Kropp, W. Baaziz, O. Ersen, D. Teschner, R. Schlögl, M. Mavrikakis and S. Zafeiratos, *ACS Catal.*, 2019, **9**, 8325.
29 L. Wang, Y. Li, J. Liu, Z. Tian and Y. Jing, *Sep. Purif. Technol.*, 2021, **277**, 119505.
30 P. Gawade, B. Bayram, A. M. C. Alexander and U. S. Ozkan, *Appl. Catal., B*, 2012, **128**, 21.

31 Z. Zhao, M. M. Yung and U. S. Ozkan, *Catal. Commun.*, 2008, **9**, 1465.
32 M. Greluk, W. Gac, M. Rotko, G. Słowik and S. Turczyniak-Surdacka, *J. Catal.*, 2021, **393**, 159.
33 B. V. Ayodele, M. R. Khan and C. K. Cheng, *Int. J. Hydrogen Energy*, 2016, **41**, 198.
34 A. Choya, B. De Rivas, J. I. Gutiérrez-Ortiz and R. López-Fonseca, *Ind. Eng. Chem. Res.*, 2022, **61**, 17854.
35 H. M. Kim, C. H. Jeong, B. S. Cheon, S. S. Negi, W. Won and D. W. Jeong, *Energy Fuels*, 2024, **38**, 4743.
36 C. W. Tang, C. C. Kuo, M. C. Kuo, C. Bin Wang and S. H. Chien, *Appl. Catal., A*, 2006, **309**, 37.
37 M. Konsolakis, M. Sgourakis and S. A. C. Carabineiro, *Appl. Surf. Sci.*, 2015, **341**, 48.
38 X. Xu, J. Li and Z. Hao, *J. Rare Earths*, 2006, **24**, 172.
39 C. Huang, Y. Yu, X. Tang, Z. Liu, J. Zhang, C. Ye, Y. Ye and R. Zhang, *Appl. Surf. Sci.*, 2020, **532**, 147335.
40 F. Xie, S. Xu, L. Deng, H. Xie and G. Zhou, *Int. J. Hydrogen Energy*, 2020, **45**, 26938.
41 L. Savereide, S. L. Nauert, C. A. Roberts and J. M. Notestein, *J. Catal.*, 2018, **366**, 150.
42 J. Yang, N. Yigit, J. Möller and G. Rupprechter, *Chem. – Eur. J.*, 2021, **27**, 16947.
43 H. Wang, D. Mao, J. Qi, Q. Zhang, X. Ma, S. Song, L. Gu, R. Yu and D. Wang, *Adv. Funct. Mater.*, 2019, **29**, 1806588.
44 D. Jampaiah, P. Venkataswamy, V. E. Coyle, B. M. Reddy and S. K. Bhargava, *RSC Adv.*, 2016, **6**, 80541.
45 M. Xiao, X. Zhang, Y. Yang, X. Cui, T. Chen and Y. Wang, *Fuel*, 2022, **323**, 124379.
46 B. Liu, W. Li, W. Song and J. Liu, *Phys. Chem. Chem. Phys.*, 2018, **20**, 16045.
47 C. Sui, L. Xing, X. Cai, Y. Wang, Q. Zhou and M. Li, *Catalysts*, 2020, **10**, 243.
48 K. Polychronopoulou, A. A. Alkhoori, A. M. Efstathiou, M. A. Jaoude, C. M. Damaskinos, M. A. Baker, A. Almutawa, D. H. Anjum, M. A. Vasiliades, A. Belabbes, L. F. Vega, A. F. Zedan and S. J. Hinder, *ACS Appl. Mater. Interfaces*, 2021, **13**, 22391.
49 M. Á. Stegmayer, S. Irusta, E. E. Miró and V. G. Milt, *Catal. Today*, 2022, **383**, 266.
50 B. J. Wang, G. W. Chu, Y. Bin Li, X. Z. Duan, J. X. Wang and Y. Luo, *Chem. Eng. Sci.*, 2021, **244**, 116814.
51 J. Tian, W. Na, H. Wang and W. Gao, *Adv. Mater. Res.*, 2013, **643**, 76.
52 M. Kang, M. W. Song and C. H. Lee, *Appl. Catal., A*, 2003, **251**, 143.
53 C. L. Bolívar-Díaz, J. C. Conesa, V. Cortés Corberán, M. Monte and A. Martínez-Arias, *J. Nanosci. Nanotechnol.*, 2017, **17**, 3816.
54 M. S. Yakimova, V. K. Ivanov, O. S. Polezhaeva, A. A. Trushin, A. S. Lermontov and Y. D. Tretyakov, *Dokl. Chem.*, 2009, **427**, 186.
55 Y. Park, S. K. Kim, D. Pradhan and Y. Sohn, *Chem. Eng. J.*, 2014, **250**, 25.
56 M. Lykaki, E. Papista, N. Kaklidis, S. A. C. Carabineiro and M. Konsolakis, *Catalysts*, 2019, **9**, 233.
57 M. Thommes, K. Kaneko, A. V. Neimark, J. P. Olivier, F. Rodriguez-Reinoso, J. Rouquerol and K. S. W. Sing, *Pure Appl. Chem.*, 2015, **87**, 1051.
58 S. Stefa, M. Lykaki, G. Varvoutis, M. Zografaki, V. D. Binas, G. E. Marnellos and M. Konsolakis, *Sustainable Chem. Environ.*, 2025, **10**, 100243.
59 D. D. M. Prabaharan, K. Sadaiyandi, M. Mahendran and S. Sagadevan, *Appl. Phys. A: Mater. Sci. Process.*, 2017, **123**, 264.
60 R. D. Shannon, *Acta Crystallogr., Sect. A*, 1976, **32**, 751.
61 A. Jeyaranjan, T. S. Sakthivel, M. Molinari, D. C. Sayle and S. Seal, *Part. Part. Syst. Charact.*, 2018, **35**, 1800176.
62 Y. Lin, Z. Wu, J. Wen, K. R. Poeppelmeier and L. D. Marks, *Nano Lett.*, 2013, **14**, 191.
63 Y. Pang, J. Tong, X. Fan, D. Yang, Z. Chen, L. Zhou and B. Yan, *J. Mater. Sci.*, 2024, **59**, 13462.
64 Y. Liu, B. Hou, L. Jia, C. Chen, Z. Ma, J. Wang and D. Li, *Fuel*, 2022, **324**, 124518.
65 J. M. López, A. L. Gilbank, T. García, B. Solsona, S. Agouram and L. Torrente-Murciano, *Appl. Catal., B*, 2015, **174–175**, 403.
66 G. Grzybek, P. Stelmachowski, S. Gudyka, P. Indyka, Z. Sojka, N. Guillén-Hurtado, V. Rico-Pérez, A. Bueno-López and A. Kotarba, *Appl. Catal., B*, 2016, **180**, 622.
67 X. Yao, Y. He, S. Fu, X. Yang, S. Cui, L. Cheng, Y. Pan and Z. Jiao, *Catal. Commun.*, 2023, **179**, 106687.
68 Ravina, S. Dalela, S. Kumar, B. L. Choudhary and P. A. Alvi, *Mater. Today: Proc.*, 2023, **79**, 165.
69 V. G. Hadjiev, M. N. Iliev and I. V. Vergilov, *J. Phys. C: Solid State Phys.*, 1988, **21**, L199.
70 L. Ilieva, P. Petrova, A. M. Venezia, E. M. Anghel, R. State, G. Avdeev and T. Tabakova, *Catalysts*, 2021, **11**, 1316.
71 I. E. Wachs, *Catal. Today*, 1996, **27**, 437.
72 J. Y. Luo, M. Meng, X. Li, X. G. Li, Y. Q. Zha, T. D. Hu, Y. N. Xie and J. Zhang, *J. Catal.*, 2008, **254**, 310.
73 J. Liu, Z. Zhao, J. Wang, C. Xu, A. Duan, G. Jiang and Q. Yang, *Appl. Catal., B*, 2008, **84**, 185.
74 D. G. Araiza, C. A. Celaya, A. Gómez-Cortés, S. Tehuacanero-Cuapa, J. N. Díaz de León, J. Muñiz, H. A. Lara-García and G. Díaz, *Top. Catal.*, 2022, **65**, 1331.
75 Y. Wang, X. Hu, K. Zheng, H. Zhang and Y. Zhao, *React. Kinet., Mech. Catal.*, 2018, **123**, 707.
76 L. Wang and H. Liu, *Catal. Today*, 2018, **316**, 155.
77 S. W. Yu, H. H. Huang, C. W. Tang and C. Bin Wang, *Int. J. Hydrogen Energy*, 2014, **39**, 20700.
78 S. Kumar Megarajan, S. Rayalu, Y. Teraoka and N. Labhsetwar, *J. Mol. Catal. A: Chem.*, 2014, **385**, 112.
79 F. Hu, Y. Peng, J. Chen, S. Liu, H. Song and J. Li, *Appl. Catal., B*, 2019, **240**, 329.
80 M. A. Vasiliades, C. M. Damaskinos, M. Lykaki, S. Stefa, V. D. Binas, T. Kentri, S. Boghosian, M. Konsolakis and A. M. Efstathiou, *Appl. Catal., B*, 2024, **350**, 123906.
81 G. H. Jaffari, A. Imran, M. Bah, A. Ali, A. S. Bhatti, U. S. Qurashi and S. Ismat Shah, *Appl. Surf. Sci.*, 2017, **396**, 547.
82 Y. Deng, J. Gao, A. Zhao, W. Song, W. Yin, J. He, L. Yang, L. Yuan, Y. Wang and L. Ouyang, *Ind. Eng. Chem. Res.*, 2025, **64**, 8642.

83 L. Wang, S. Deo, K. Dooley, M. J. Janik and R. M. Rioux, *Chin. J. Catal.*, 2020, **41**, 951.

84 W. W. Wang, W. Z. Yu, P. P. Du, H. Xu, Z. Jin, R. Si, C. Ma, S. Shi, C. J. Jia and C. H. Yan, *ACS Catal.*, 2017, **7**, 1313.

